AIAA JOURNAL
Vol. 34, No. 12, December 1996

Simulation of Turbulent Square-Duct Flow: Dissipation and Small-Scale Motion

Asmund Huser* and Sedat Biringen†
University of Colorado, Boulder, Colorado 80309-0429

Results and the database from a direct numerical simulation of turbulent flow in a square duct are used to investigate the dissipation processes in a flow with two inhomogeneous directions. First, the effect of the corner on small-scale topological patterns is identified, and second, information for the assessment and development of turbulence closure models is provided by calculating all of the terms in the transport equations for the turbulent dissipation rate and enstrophy. It is shown that, with the exception of two production terms, these budgets have the same dynamics down to the wall. The effects of the corner are manifested by vanishing turbulence production in the viscous sublayer very close to the corner, and reduced dissipation of turbulent vorticity along the diagonal, farther away from the corner.

I. Introduction

DIRECT numerical simulation (DNS) of simple shear flows has proven to be an effective and important tool for studying turbulence structures and near-wall effects.[1] The present paper extends this idea to complex turbulent flows by using the database from a recent DNS of turbulent square-duct flow[2] to investigate the influence of the corner on the structure of small-scale turbulence. These effects are manifested by vanishing turbulence production as well as reduced turbulence energy and dissipation along the diagonal (corner bisector).[2] The imbalance between the turbulence along the corner bisector and the midchannel (wall bisector) creates the stress-driven secondary flow, defined as secondary flow of the second kind.[2-4]

Of particular interest in this paper is the turbulence dissipation-rate (and enstrophy) budget because the dissipation rate contributes significantly to the Reynolds stress balance.[3] An order-of-magnitude analysis of the dissipation process is provided by Tennekes and Lumley[5] by estimating the terms in the turbulence enstrophy budget. Mansour et al.[6] presented all of the terms in the dissipation-rate budget from the DNS of turbulent channel flow and demonstrated the significance of these terms in a wall-bounded flow. The work of Rodi and Mansour[7] also indicates the importance of all terms in the dissipation-rate budget near the wall, including the transport and diffusion.

Because of their connection to the dissipation processes,[8] the small-scale topological structures also are considered. By displaying scatter plots of the invariants of the local deformation tensor obtained in the homogeneous direction and in time, we can deduce the preferred small-scale topologies and dissipation production processes in the square duct.

The present results document all of the terms in the turbulence dissipation rate and enstrophy equations that are essential for both the modeling of Reynolds stress transport equations and the development of subgrid-scale models.

II. Solution Procedure

The present results are generated from a DNS of turbulent flow in a square duct. The numerical solution of the Navier–Stokes equations incorporates a time-splitting method and the decoupled equations are solved semi-implicitly by a Runge–Kutta procedure. In the wall-normal directions, spatial discretization is done by fifth-order upwind biased finite differences for the convective terms[9] and fourth-order finite differences for all other terms. In the duct (streamwise) direction, periodic boundary conditions are applied (for details, see Refs. 3 and 4).

The calculations were performed in the fully developed turbulent regime at a Reynolds number $Re_\tau = u_\tau D/\nu = 600$, where u_τ is the mean friction velocity and D is the duct width; the bulk Reynolds number was $Re_B = U_B D/\nu = 1.032 \times 10^4$, where U_B is the bulk velocity.

The governing equations were normalized by u_τ and D and can be written as

$$\frac{\partial \boldsymbol{u}}{\partial t} + \boldsymbol{u} \cdot \nabla \boldsymbol{u} = -\nabla p + \frac{1}{Re_\tau} \nabla^2 \boldsymbol{u} + 4\boldsymbol{i} \tag{1}$$

$$\nabla \cdot \boldsymbol{u} = 0 \tag{2}$$

where $4\boldsymbol{i}$ is the nondimensional driving pressure gradient. The computational mesh consisted of $96 \times 101 \times 101$ grid points in the x, y, z directions, respectively, where x is the streamwise direction and y and z are the wall-normal directions; the computational box length was $L_x/D = 6.4$. Statistics presented in this paper were collected during a period of $t = Tu_\tau/D = 10$ time units (T is the dimensional time) after the flow reached a statistically steady state.

A coarse-mesh simulation[3] using an $81 \times 81 \times 64$ grid yielded a mean skin friction value within 1% of the fine-mesh value, indicating the mesh independence of the present results. Note also that the fine-grid resolution of the present work is comparable to the one employed by Rai and Moin[9] in their channel-flow simulations (for hydraulic radius-based Reynolds numbers slightly higher than the present work), where they obtained good results up to third-order statistics and for the rms vorticity components. Finally, a comparison of the rms vorticity distributions from the present results along the wall bisector with high-resolution channel-flow simulations[10] and boundary-layer experimental data[11] provide good agreement (Fig. 1). Good agreement also is obtained for the

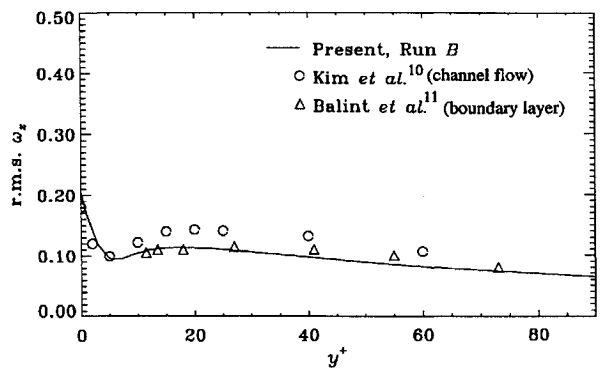

Fig. 1 Comparison of rms ω_x distributions along the wall bisector with channel flow and boundary layer flow.

Received March 1, 1995; revision received May 9, 1996; accepted for publication Aug. 2, 1996; also published in *AIAA Journal on Disc*, Volume 2, Number 1.

*Graduate Research Assistant, Department of Aerospace Engineering Sciences; currently Senior Research Scientist, Det Norske Veritas Industri Norge AS, Nøvik, Norway.

†Professor, Department of Aerospace Engineering Sciences. Associate Fellow AIAA.

dissipation-rate budget terms along the wall bisector compared with the same data. These comparisons indicate that all small-scale effects that are characteristic for wall-bounded flows are captured in the present simulations. The present dissipation-rate budget shows an imbalance of, at most, 20% of the largest term, providing an estimate of the possible uncertainty of the higher-order velocity gradient statistics.

III. Topology of Small-Scale Motion

Complex unsteady flowfields are frequently examined by considering the small-scale topology surrounding a fluid particle.[8] Perry and Chong[12] applied the critical-point theory to describe fluid motion by expanding the velocity vector u_i in terms of a Taylor series around a given point O in the flowfield. Neglecting higher-order terms in the Taylor series, the deformation tensor, $A = \partial\tilde{u}_i/\partial x_j$, describes the topology, and in a Lagrangian framework, the characteristic equation for A describes the topology of the small-scale motion. Accordingly, the first, second, and third invariants of the characteristic equation for the deformation tensor, P, Q, and R, respectively, can be employed to obtain expressions for the dissipation rate of kinetic energy and other physical mechanisms.

Because $P = 0$ in an incompressible flow, the solution of the eigensystem is given by the invariants Q and R only, so that by evaluating Q and R, the local topology can be obtained (see Ref. 13 for a detailed description of the various topologies in PQR space). In the $P = 0$ plane, the solution type is divided into two major categories by the line

$$R = \pm(2\sqrt{3}/9)(-Q)^{\frac{3}{2}} \tag{3}$$

with complex solutions above and real solutions below this line in a Q vs R plot (Fig. 2). The complex solutions (having one real and two complex conjugate eigenvalues) give particle paths going toward or away from a focus in a spiraling motion (the spiral lies in a plane perpendicular to the real eigenvector, focus/stretching or focus/compression). The real solutions are best described by three planes cutting through the particle paths, spanned by the eigenvectors; one plane contains particle paths going toward or away from a node and the two other planes contain flow around a saddle point (node/saddle/saddle).[13] The vertical line, $R = 0$, in Fig. 2 divides the topologies into those with stable solutions for $R < 0$ and unstable solutions for $R > 0$. Stable solutions involve flow toward focus or node and unstable solutions involve flow away from the focus or node.

A physical interpretation is given to the second and third invariants when the deformation tensor is divided into a symmetric and an antisymmetric part: $A = S + C$. The symmetric part is the rate-of-strain tensor $S = (A + A^T)/2$, and the antisymmetric part is the rate-of-rotation tensor $C = (A - A^T)/2$.

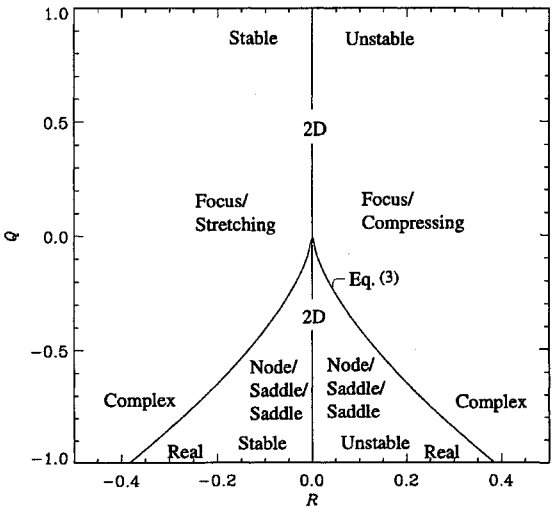

Fig. 2 Identification of local flow topologies in the plane $P = 0$.

Considering the second invariant and defining the trace as tr, this is written

$$Q = \tfrac{1}{2}(-\mathrm{tr}[S^2] - \mathrm{tr}[C^2]) \tag{4}$$

In nondimensional form, the instantaneous dissipation rate of kinetic energy reads

$$\tilde{\epsilon} = (-2/Re_B)\mathrm{tr}[S^2] = (-4/Re_B)Q_S \tag{5}$$

The total instantaneous enstrophy can be written as

$$\tilde{\omega} = \mathrm{tr}[C^2] = 2Q_C \tag{6}$$

Equations (5) and (6) are obtained when Q is split into a symmetric part Q_S and an antisymmetric part Q_C:

$$Q = Q_S + Q_C \tag{7}$$

Similarly, considering the third invariant, one obtains

$$R = \tfrac{1}{3}(-\mathrm{tr}[S^3] - 3\,\mathrm{tr}[C^2S]) \tag{8}$$

The terms in Eq. (8) can be associated with physical mechanisms, viz.,

$$\tilde{P}^4_\epsilon = (-2/3Re_B)\mathrm{tr}[S^3] = (-1/Re_B)R_S \tag{9}$$

$$\tilde{P}^4_\omega = \mathrm{tr}[C^2S] = R_C \tag{10}$$

where $R = R_S + R_C$ and $\tilde{P}^4_\epsilon$ and $\tilde{P}^4_\omega$ are instantaneous terms of the same form as P^4_ϵ and P^4_ω. These two terms contain instantaneous velocities ($\tilde{u}$) instead of the fluctuating velocity (u') and are explicitly given in Sec. V. If the mean velocity derivatives are small (i.e., away from the wall), these terms are comparable to the similar turbulent terms and hence the same physical interpretation is given. Therefore, these two terms are related to the production of dissipation and enstrophy by turbulent motion and vortex stretching, respectively. In Sec. V, the validity of comparing instantaneous and turbulent values is addressed when the terms in Eqs. (9) and (10) are Reynolds-averaged and the turbulent components are presented in connection with the turbulent dissipation-rate and enstrophy equations.

IV. Topology of Turbulent Flow in a Square Duct

In the present flowfield, the scatterplots of (Q, R) and (Q_S, R_S) pairs at given locations in the y, z plane are obtained to identify the dominant small-scale topological structures.

Figures 3 and 4 present scatterplots, where each point corresponds to a (Q, R) pair or a (Q_S, R_S) pair at a given streamwise x location and a given time instant. The scatterpoints were collected over a period $T = 20D/U_B$ after a statistically steady state was reached.

Considering the (Q, R) pairs obtained on the wall bisector and the corner bisector (Figs. 3 and 4, top panels), it is observed that outside of the viscous sublayer ($z = 0.022$), there are slight preferences for stable focus/stretching and unstable node/saddle/saddle topologies. These preferences also are found in a turbulent mixing layer,[8] with a stronger preference for stable focus/stretching topologies than in the present flow. Accordingly, the stable focus/stretching topology is characteristic for shear-driven turbulence containing vortices undergoing stretching.

At the corner bisector, near the edge of the viscous sublayer (Fig. 4, $y = z = 0.022$), the same topology preferences are observed as along the wall bisector (Fig. 3, $y = 0.022, z = 0.5$), indicating that near the edge of the viscous sublayer ($y^+ \approx 13$) the small-scale turbulence structures are not altered by the intersecting wall; however, the absolute values of the invariants are reduced near the corner. This magnitude reduction is due to the reduced turbulence intensity in this region.

If one considers the topology of the symmetric part of the deformation tensor, the (Q_S, R_S) pairs along the wall bisector reveal that, outside the viscous sublayer, high negative Q_S values are correlated with high positive R_S values, so that high dissipation events are associated with unstable nodes (Fig. 3, bottom). This also is observed in a turbulent mixing layer,[8] where the relation

$$R_S \approx K(-Q_S)^{\frac{3}{2}} \tag{11}$$

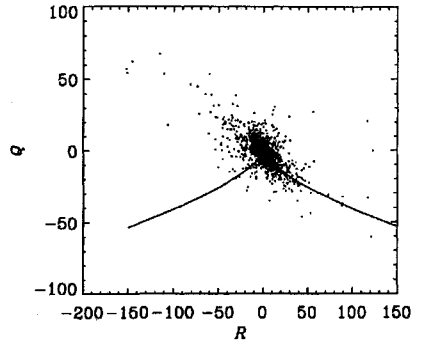

Q vs R

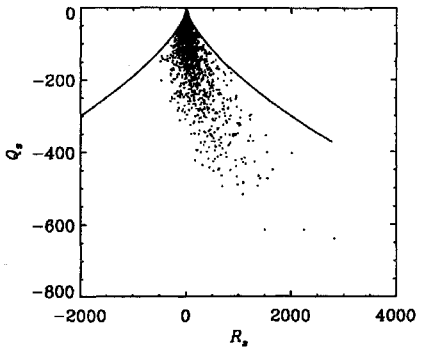

Q_S vs R_S

Fig. 3 Scatterplots at $y, z = 0.5, 0.022$.

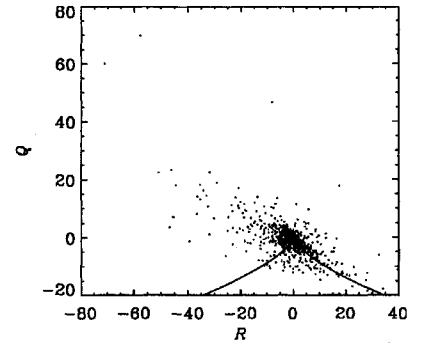

Q vs R

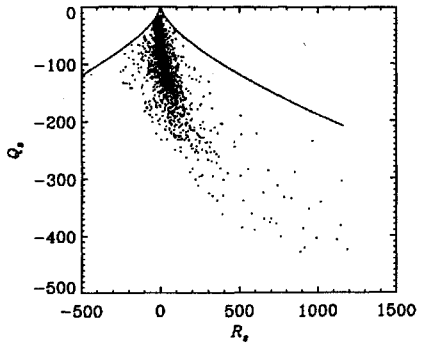

Q_S vs R_S

Fig. 4 Scatterplots at $y, z = 0.022, 0.022$.

is found to be valid even though the bulk of the dissipation events is concentrated near the origin in the Q_S, R_S plane. Here, K is a constant with an upper limit of $K = 2\sqrt{3}/9$ [see Eq. (3)]. The relation given by Eq. (11) seems to be valid also in the core of the square-duct flow. Low dissipation events (corresponding to $-Q_S$ events close to zero) are most frequent in the core of the square duct as well as in the mixing layer.

In the high turbulence production region in the square-duct flow, dissipation increases at the wall bisector by about two orders of magnitude compared to dissipation in the core of the flow, and the dissipation events are concentrated below the origin on both sides of the line $R_S = 0$ in the $-Q_S$, R_S scatterplots (Fig. 3, bottom). For the extreme high dissipation events in the high turbulence production region, Eq. (11) is still valid, indicating that these extreme events are caused by vortex stretching. For the bulk of the dissipation events, effects other than vortex stretching take place.

For high Reynolds numbers, an order-of-magnitude analysis[5] of the turbulent enstrophy and the dissipation rate terms gives $-Q_S \simeq Q_R$. The scatterplot of these quantities presented by Huser[4] indicates that enstrophy and dissipation also are well correlated in the corner region. Note further that the boundary conditions and the continuity equation give $-Q_S = Q_R$ at the wall. Therefore, the instantaneous dissipation rate and enstrophy are similar in the whole duct. In the transitional mixing layer,[8] high enstrophy (Q_R) is correlated with high dissipation ($-Q_S$), but high enstrophy also is correlated with low dissipation, which is not observed in the present flow.

V. Dissipation Rate and Enstrophy Budgets

The dissipation rate tensor

$$\epsilon_{ij} = 2\overline{\frac{\partial u_i'}{\partial x_k}\frac{\partial u_j'}{\partial x_k}} \tag{12}$$

is one of the dominant terms in the Reynolds stress budget, both near the wall and far from the wall. The transport equations for ϵ_{ij} consist of four additional transport equations for the square-duct flow. In most turbulence closures, near-isotropic behavior of the dissipation-rate tensor is assumed, and only the trace of the transport equations for ϵ_{ij} is considered, providing a transport equation for the dissipation rate of turbulent kinetic energy, $\epsilon = \epsilon_{ii}/2$. The anisotropic behavior of the individual terms in ϵ_{ij} is usually modeled algebraically in terms of ϵ, k, and τ_{ij}, where $\tau_{ij} = \overline{u_i u_j}$ represents the anisotropy.[14]

The transport equation for ϵ is given by

$$\frac{\partial \epsilon}{\partial t} + \bar{u}_k \nabla_k \epsilon = P_\epsilon^1 + P_\epsilon^2 + P_\epsilon^3 + P_\epsilon^4 + \Pi_\epsilon + T_\epsilon - Y_\epsilon + \nabla^2 \epsilon \tag{13}$$

where the terms on the right-hand side of Eq. (13) are written as[6]

$$P_\epsilon^1 = -\epsilon_{ik} A_{ik} \qquad \text{(mixed production)} \tag{14}$$

$$P_\epsilon^2 = -2\overline{\frac{\partial u_j'}{\partial x_i}\frac{\partial u_j'}{\partial x_k}} A_{ik} \qquad \text{(production by mean velocity gradient)} \tag{15}$$

$$P_\epsilon^3 = -2\overline{u_k' \frac{\partial u_i'}{\partial x_j}} \frac{\partial^2 \bar{u}_i}{\partial x_k \partial x_j} \qquad \text{(gradient production)} \tag{16}$$

$$P_\epsilon^4 = -2\overline{\frac{\partial u_i'}{\partial x_k}\frac{\partial u_i'}{\partial x_m}\frac{\partial u_k'}{\partial x_m}} \qquad \text{(turbulent production)} \tag{17}$$

$$\Pi_\epsilon = -\nabla_i \cdot \overline{\frac{\partial p'}{\partial x_m}\frac{\partial u_i'}{\partial x_m}} \qquad \text{(pressure transport)} \tag{18}$$

$$T_\epsilon = -\nabla_i \cdot \overline{u_i' \frac{\partial u_k'}{\partial x_m}\frac{\partial u_k'}{\partial x_m}} \qquad \text{(turbulent transport)} \tag{19}$$

$$Y_\epsilon = 2\overline{\frac{\partial^2 u_i'}{\partial x_k \partial x_m}\frac{\partial^2 u_i'}{\partial x_k \partial x_m}} \qquad \text{(destruction of dissipation)} \tag{20}$$

and $A_{ij} = \partial \bar{u}_i / \partial x_j$ is the mean deformation tensor. Equation (13) is written in $\{\}^+$ variables, and each term represents a transport rate, involving the use of u_τ and ν/u_τ as the velocity scale and the length scale, respectively. When presenting distributions of these terms, both y and y^+ coordinates are used, with y^+ defined as

$$y^+ = yRe_\tau \tag{21}$$

where $y = Y/D$ and Y is the dimensional coordinate.

After averaging in x and t (so that x and t derivatives of mean quantities vanish), distribution plots of all of the remaining terms

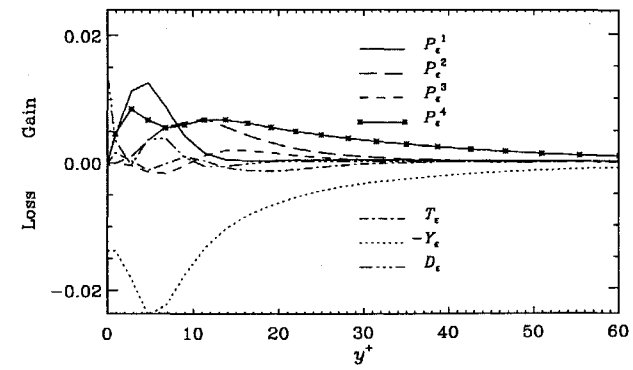

a) $z = 0.50$

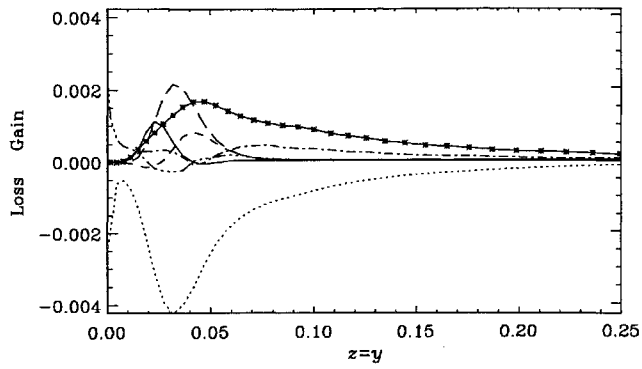

b) Corner bisector

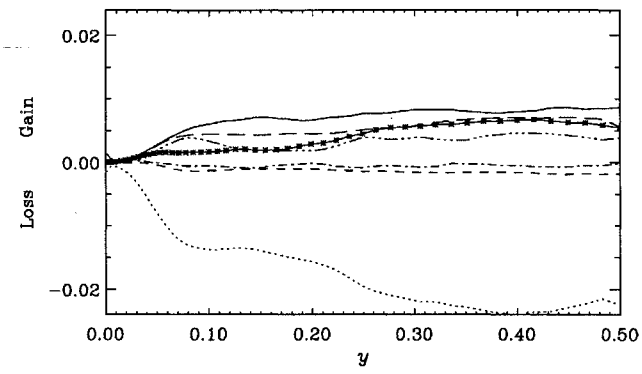

c) $z = 0.011$

Fig. 5 Ensemble-averaged dissipation-rate budget distributions at different locations.

in Eq. (13) in the inhomogeneous y, z plane are presented (Fig. 5). Pressure transport was found to be negligible and is not plotted (in accordance with results from channel flow[7]).

The effects of the corner are disclosed when the budget terms are plotted along the corner bisector in Fig. 5b, demonstrating that the maximum value in P_ϵ^4 near the wall disappears and the relative magnitude of P_ϵ^1 is reduced. Also, in the corner, the local minimum value in $-Y_\epsilon$ at the wall is captured. A small contribution from T_e provides increased dissipation along the corner bisector.

Outside the viscous sublayer, along the corner bisector, the same dissipation processes occur as those immediate outside the viscous sublayer at the wall bisector. In the viscous layer (along the corner bisector), in contrast to wall flow, no peaks in P_ϵ^1 and P_ϵ^4 occur; this is due to the vanishing turbulence production here. Note that the dissipation-rate distribution near the wall is characterized by the two maximum values, one at the wall, and the other (local) at the production peak ($y^+ = 12$). The two effects responsible for these maxima are also displayed in the dissipation-rate budget (Fig. 5a) by the two maximum values in P_ϵ^4 and the strong P_ϵ^1 and $-Y_\epsilon$ at $y^+ \approx 5$. In the region between the production peaks of P_ϵ^1 and P_ϵ^2 [$y^+ \approx 8$ (Fig. 5)], the diffusion rates, T_ϵ and $\nabla^2\epsilon$ (represented by D_ϵ in Fig. 5a) are positive. This area of positive diffusion separates the regions where turbulent and viscous effects are dominant, corresponding to the edge of the viscous sublayer. The influence of the intersecting wall on the production of dissipation is clearly displayed by plotting the distributions along the mixed production P_ϵ^1 ridge at $z = 0.011$(corresponding to the P_ϵ^1 maximum at $y^+ \approx 5$) following the vertical wall (Fig. 5c). The influence of the horizontal wall on P_ϵ^4 starts around $y = 0.2$ by a decrease in P_ϵ^4, and the viscous effects do become important around $y = 0.1$ with a decrease in P_ϵ^1. It is seen that P_ϵ^1, P_ϵ^2, and P_ϵ^3 are dominated by the viscous scales, and P_ϵ^4 is dominated by turbulent scales, whereas Y_ϵ is dominated by both scales. Convection of dissipation is relatively small, similar to convection of turbulent kinetic energy.[4]

Typical for inhomogeneous flows, (Q, R) pairs are located close to origin in Fig. 2, causing enstrophy and dissipation to be well correlated; it is suggested that this correlation is universal.[8] The instantaneous dissipation rate and enstrophy also were found to be well correlated, in the corner region,[4] similarly for the Reynolds-averaged values:

$$\epsilon \simeq \omega \tag{22}$$

where $\omega = \overline{\omega_i'\omega_i'}$ is the mean-square vorticity fluctuation or the turbulent enstrophy. Equation (22) is written in $\{\}^+$ variables so that the dependence of viscosity is not explicitly displayed. The result given by Eq. (22) was further investigated by Huser[4] by comparing the terms in the dissipation-rate equation with the terms in the turbulent enstrophy equation for the square-duct flow. The turbulent enstrophy equation is derived from the fluctuating vorticity equation and contains terms that are similar to the terms in the dissipation-rate equation,

$$\frac{\partial \omega}{\partial t} + \bar{u}_k \nabla_k \omega = P_\omega^1 + P_\omega^2 + P_\omega^3 + P_\omega^4 + T_\omega - Y_\omega + \nabla^2\omega \tag{23}$$

the explicit form of these terms is available elsewhere.[4,5] When comparing each of the terms in the ω equation with the corresponding terms in the ϵ equation, the following relations can be obtained[4]:

$$P_\omega^1 + P_\omega^2 \simeq P_\epsilon^1 + P_\epsilon^2 \tag{24}$$

$$P_\omega^3 \simeq P_\epsilon^3 \tag{25}$$

$$P_\omega^4 \simeq P_\epsilon^4 \tag{26}$$

$$T_\omega \simeq T_\epsilon \tag{27}$$

$$Y_\omega \simeq Y_\epsilon \tag{28}$$

The third relation, Eq. (26), also was found in the topology analysis (Sec. IV) for the instantaneous values, and this result (for the turbulent quantities) is not surprising because the strain rate and vorticity fluctuations are much larger than their respective mean values. In the present flow, the rms vorticity components are about 10 times larger than the maximum value of the mean streamwise vorticity away from the wall. At the wall, however, rms and mean values of vorticity are comparable.

The only differences between the ϵ and the ω budgets are in the first two production terms, even though their sum is similar (Eq. 24). The distribution of the budget terms along the wall bisector shows that P_ω^1 is the dominant production term in the viscous sublayer and that P_ω^2 has a smaller loss in the viscous sublayer and a gain near the turbulence production maximum, at $y^+ = 12$ (Fig. 6a). The distributions along the corner bisector (Fig. 6b) reveal that also for the ω budget, production is due to turbulent effects. In the viscous sublayer in the corner, all of the production gradients vanish, and production of enstrophy by P_ω^1 and P_ω^4 takes place around the turbulence production region ($y^+ \approx 12$). The mixed production, P_ω^1, provides a loss of ω outside the viscous sublayer, and this loss amplifies near the corner (see Fig. 6b, solid line). Note that P_ω^1 and P_ω^2 have opposite effects, contrary to P_ϵ^1 and P_ϵ^2.

The similar dynamics of the dissipation-rate and the enstrophy budgets confirms that the enstrophy budget also can be considered when developing turbulence models for the dissipation rate in the wall region. Especially the behavior of the first two production terms

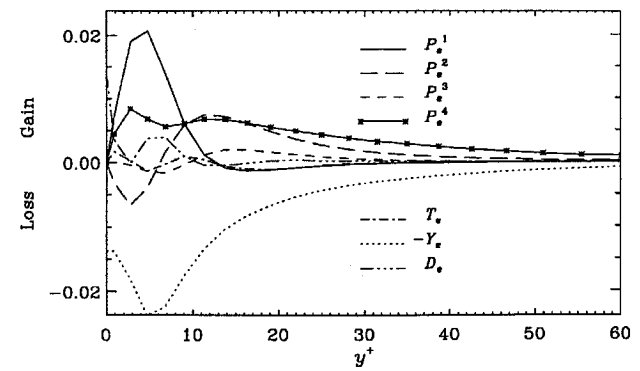

a) z = 0.05

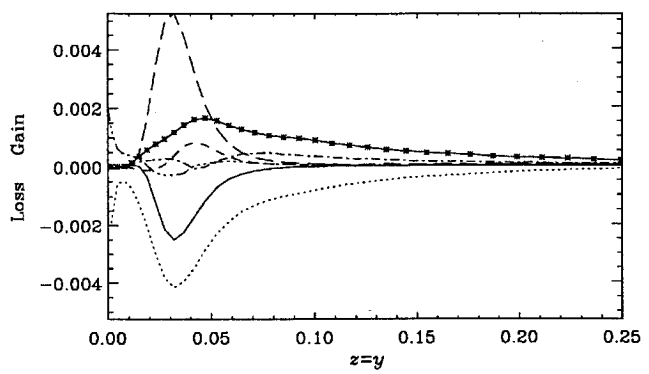

b) Corner bisector

Fig. 6 Ensemble-averaged turbulent enstrophy budget distributions at different locations.

(Eq. 24) may shed some light on the modeling of the two first production terms in the dissipation-rate budget because of their different behavior and the link between the turbulent and the mean enstrophy budgets.[5]

VI. Conclusions

The database from a DNS of fully developed turbulent flow in a square duct is employed to perform a topology analysis and to find all of the terms in the dissipation-rate and enstrophy transport equations.

By considering the symmetric part of the strain-rate tensor, it is inferred from the topology analysis that the effect of the wall reduces the correlation between production of dissipation by vortex stretching and dissipation itself, indicating that other production terms must be present. The small-scale topology patterns obtained from the invariants of the deformation tensor are comparable to patterns in other inhomogeneous flows, manifested by invariants close to zero in the whole duct.

The dissipation-rate ϵ and turbulent-enstrophy ω transport equations are considered. The strong production of dissipation in the viscous sublayer vanishes in the corner, and the gradients at the wall for these production terms become zero in the near vicinity of the corner. The dominant production of dissipation in the corner is due to turbulence effects, most likely old eddies that were produced at the walls, dissipating as they pass the corner bisector. The similarity between the dynamics of the dissipation rate and the turbulent enstrophy is shown, and practically no difference in the distributions of the terms in the ϵ and the ω budgets is observed. The only differences in these budgets are in the two first production terms, which may shed some light on the modeling of the dissipation rate because these terms provide two different representations of the same effect.

Acknowledgments

The first author acknowledges the Fulbright Foundation, the Norwegian Space Agency, and the Royal Norwegian Council for Scientific and Industrial Research for financial support. Also acknowledged is Cray Research for providing computer time. Partial support for this study was provided by Office of Naval Research Grant N00014-91-J-1086 with J. A. Fein as the Technical Monitor.

References

[1]Reynolds, W. C., "The Potential and Limitations of Direct and Large Eddy Simulations," *Whither Turbulence? or Turbulence at the Crossroads*, Vol. 357, Lecture Notes in Physics, Springer–Verlag, Berlin, 1990, pp. 313–343.

[2]Huser, A., and Biringen, S., "Direct Numerical Simulation of Turbulent Flow in a Square Duct," *Journal of Fluid Mechanics*, Vol. 257, 1993, pp. 65–95.

[3]Huser, A., Biringen, S., and Hatay, F. F., "Direct Simulation of Turbulent Flow in a Square Duct: Reynold Stress Budgets," *Physics of Fluids*, Vol. 6, No. 9, 1994, pp. 3144–3152.

[4]Huser, A., "Direct Numerical Simulation of Turbulent Flow in a Square Duct," Ph.D. Thesis, Dept. of Aerospace Engineering Sciences, Univ. of Colorado, Boulder, CO, 1992.

[5]Tennekes, H., and Lumley, J. L., *A First Course in Turbulence*, MIT Press, Cambridge, MA, 1972.

[6]Mansour, N. N., Kim, J., and Moin, P., "Reynolds-Stress and Dissipation Rate Budgets in a Turbulent Channel Flow," *Journal of Fluid Mechanics*, Vol. 194, 1988, pp. 15–44.

[7]Rodi, W., and Mansour, N. N., "Modeling the Dissipation-Rate Equation with the Aid of Direct Numerical Simulation," *Studies in Turbulence*, Springer–Verlag, New York, 1992, pp. 17–38.

[8]Soria, J., Sondregaard, R., Cantwell, B. J., Chong, M. S., and Perry, A. E., "A Study of the Fine-Scale Motions of Incompressible Time-Developing Mixing Layers," *Physics of Fluids*, Vol. 6, No. 2, 1994, pp. 871–884.

[9]Rai, M. M., and Moin, P., "Direct Simulation of Turbulent Flow Using Finite Difference Schemes," *Journal of Computational Physics*, Vol. 96, 1991, p. 15–53.

[10]Kim, J., Moin, P., and Moser, R., "Turbulence Statistics in Fully Developed Channel Flow at Low Reynolds Number," *Journal of Fluid Mechanics*, Vol. 177, 1987, p. 133–166.

[11]Balint, J.-L., Wallace, J. M., and Vukoslavčević, P., "The Velocity and Vorticity Vector Fields of a Turbulent Boundary Layer Part 2: Statistical Properties," *Journal of Fluid Mechanics*, Vol. 228, 1991, pp. 53–86.

[12]Perry, A. E., and Chong, M. S., "A Description of Eddying Motion and Flow Patterns Using Critical-Point Concepts," *Annual Review of Fluid Mechanics*, Vol. 19, 1987, pp. 125–155.

[13]Chong, M. S., and Perry, A. E., "A General Classification of Three-Dimensional Flow Fields," *Physics of Fluids*, Vol. 2, 1990, pp. 765–777.

[14]Hanjalic, K., and Launder, B. E., "Contribution Towards a Reynolds-Stress Closure for Low-Reynolds-Number Turbulence," *Journal of Fluid Mechanics*, Vol. 74, Pt. 4, 1976, pp. 593–610.